processes

MDPI

Article

Semi-Analytical Modeling of Pyrolysis Front and Ignition Temperatures of Thermally Reactive Single Solid Particles

Yousef Haseli

Central Michigan University, Mount Pleasant, MI 48859, USA; yousef@haselinnovation.com

Abstract: A semi-analytical approach is developed for predicting pyrolysis front temperature in a charring solid undergoing thermal decomposition. The pre-reaction heating stage is described using an analytical formulation and invoking the concept of thermal penetration depth. The solution for the solid conversion stage accounts for decomposition enthalpy, the convective flow of volatiles, and a reaction front characterized by a uniform temperature that progresses toward the inner layers. This method incorporates empirical relations into the analytical model. Two scenarios are considered. First, the solution of the pyrolysis model combined with the data of conversion time versus external heat flux leads to an algebraic expression that reveals the existence of a maximum pyrolysis-front temperature. Explicit relations are derived for both the extremum pyrolysis temperature and optimum applied heat flux. In the second case, an expression is derived for the ignition temperature of a solid fuel (e.g., wood) by incorporating ignition delay time measurements into the heating stage model. The newly derived expression allows the ignition temperature to be described as a function of the Biot number and external heat flux. The relation obtained for the ignition temperature explains the experimental trends reported in some previous studies where two local extremums were observed for the ignition temperature in the absence of volatile reactions.

Keywords: reaction-front temperature; ignition temperature; modeling; thermally reactive solid; pyrolysis; extremum temperature

Citation: Haseli, Y. Semi-Analytical Modeling of Pyrolysis Front and Ignition Temperatures of Thermally Reactive Single Solid Particles. *Processes* **2023**, *11*, 2448. https://doi.org/10.3390/pr11082448

Academic Editor: Antoni Sanchez

Received: 11 July 2023
Revised: 28 July 2023
Accepted: 8 August 2023
Published: 14 August 2023

1. Introduction

Thermochemical decomposition of solid materials, e.g., wood, is a complex process as it includes several chemical reactions, heat and mass transfer processes that take place concurrently. The solid decomposition may be described mathematically with a system of partial differential equations (PDEs) that would account for the conservation of energy, species mass, and momentum [1–11]. It is a challenging to nearly impossible task to analytically solve the system of PDEs that consist of conduction, reaction, and convection terms. The model equations are often solved using numerical techniques allowing the prediction of the species concentrations and the temperature of a decomposing solid.

The numerical solution of a system of nonlinear PDEs is inherently expensive computationally; this has promoted simplified (or reduced) models that account for the key aspects of the phenomena. Solving a PDE problem analytically becomes even more challenging when the solution is constrained to satisfy a specified set of initial and boundary conditions, which is the case in most physical and chemical processes such as heating a finite-size object, combustion of a solid fuel [12–16], and pyrolysis of wood.

A class of simplified models postulates that the reaction occurs at a thin layer that divides the solid into a charred region and a virgin region. The reaction front characterized by temperature T_r is first formed at the surface of the solid and then propagates toward the center. A subgroup of models based on thin reaction front accounts for solid decomposition rate using a single-step kinetic model [17,18], whereas models assuming an infinite reaction rate have also been developed [19–23]. The reaction-front temperature is predictable in the former through a combined solution of heat transfer and kinetic models, and it is

shown to vary during the process [17]. However, the latter subgroup of simplified models requires a knowledge of the reaction-front temperature often treated as a constant parameter throughout the solid decomposition.

A past study on wood pyrolysis [24] has revealed that the reaction-front temperatures obtained from the two methods (finite-rate and infinite-rate kinetics) may not be necessarily identical. Indeed, the reaction-front temperature in the infinite-rate kinetics model may be viewed as an average volumetric decomposition temperature. The question of what value should be assigned to this temperature in infinite-rate models then arises. Park et al. [25] have investigated this problem for pyrolyzing thermally thick wood. They examined the (average volumetric) pyrolysis-front temperature by means of numerical modeling and comparing the predictions of a single-step finite-rate model and a constant reaction-front temperature model where both models were developed based on the thin reaction-front approximation. The pyrolysis-front temperature was determined by equating the energy consumed by the volatiles obtained using the two models. They studied the effects of various parameters such as sample size, external heat flux, and thermal properties on the pyrolysis-front temperature.

The approach employed in the previous studies [24,25] is numerical in that one can graphically observe the effects of process parameters on the pyrolysis-front temperature. On the contrary, the present article aims to develop a closed-form solution for the pyrolysis-front temperature of a thermally reactive charring solid by solving the unsteady heat transfer equation for a finite-size solid slab. The method will assume an infinite-rate reaction taking place at a thin layer—the reaction front. The solution will lead to a relation between the total reaction time, the average reaction-front temperature, and the external heat flux. The pyrolysis-front temperature will then be expressed as a function of the applied heat flux by eliminating the reaction time using a correlation between the reaction time and the applied heat flux.

The second objective of this article is to establish a theoretical framework for a better understanding of the ignition (not necessarily the same as the onset of pyrolysis) of decomposing solids. Experimental studies have shown that the ignition temperature of solid fuels depends on numerous factors such as external heat flux, size, and solid material [26–28]. A review by Babrauskas [29] reveals that the temperature at which wood begins to react is in the range 210–497 °C, although a lower value of 190 °C has also been reported [28]. A recent study by Bartlett et al. [30] suggests that the critical heat flux at which wood ignites lies between 10 and 28 kW/m^2 with ignition temperature within 190–408 °C. Kashiwagi's extensive study [31–33] on the ignition of wood (red oak) and polymethyl methacrylate (PMMA) has shown that under identical radiant heat fluxes, autoignition takes longer than pilot ignition, and horizontally oriented samples ignite faster than vertically oriented samples.

Past modeling studies on the ignition of solid fuels often treat ignition temperature as an input parameter that corresponds to a critical heat flux; see for instance [27,34,35]. In the present article, we will derive an explicit expression for the ignition temperature as a function of the external heat flux. The method will include establishing a relation between the surface temperature at ignition, ignition delay time, and the external heat flux. Experimental studies have shown that the ignition time is inversely proportional to the applied heat flux [26,30,36–38]. This will allow the elimination of the ignition time and the derivation of an expression for the ignition temperature as a function of the external heat flux. The predictability of the expressions obtained for the pyrolysis-front temperature and ignition temperature will be qualitatively assessed against the findings of previous studies.

2. Solid Decomposition Model

Consider a solid slab whose surface receives heat from its surroundings whereas its back face is insulated. Figure 1 shows the various stages of the decomposition of a thermally thin solid that is initially at a uniform temperature. The solid is heated up until its surface temperature rises to a reaction temperature at which the solid begins to decompose. The heating phase consists of (i) the thermal penetration stage and (ii) the post-penetration stage.

The formulation to be presented employs the concept of thermal penetration depth [39] and thin reaction-front approximation.

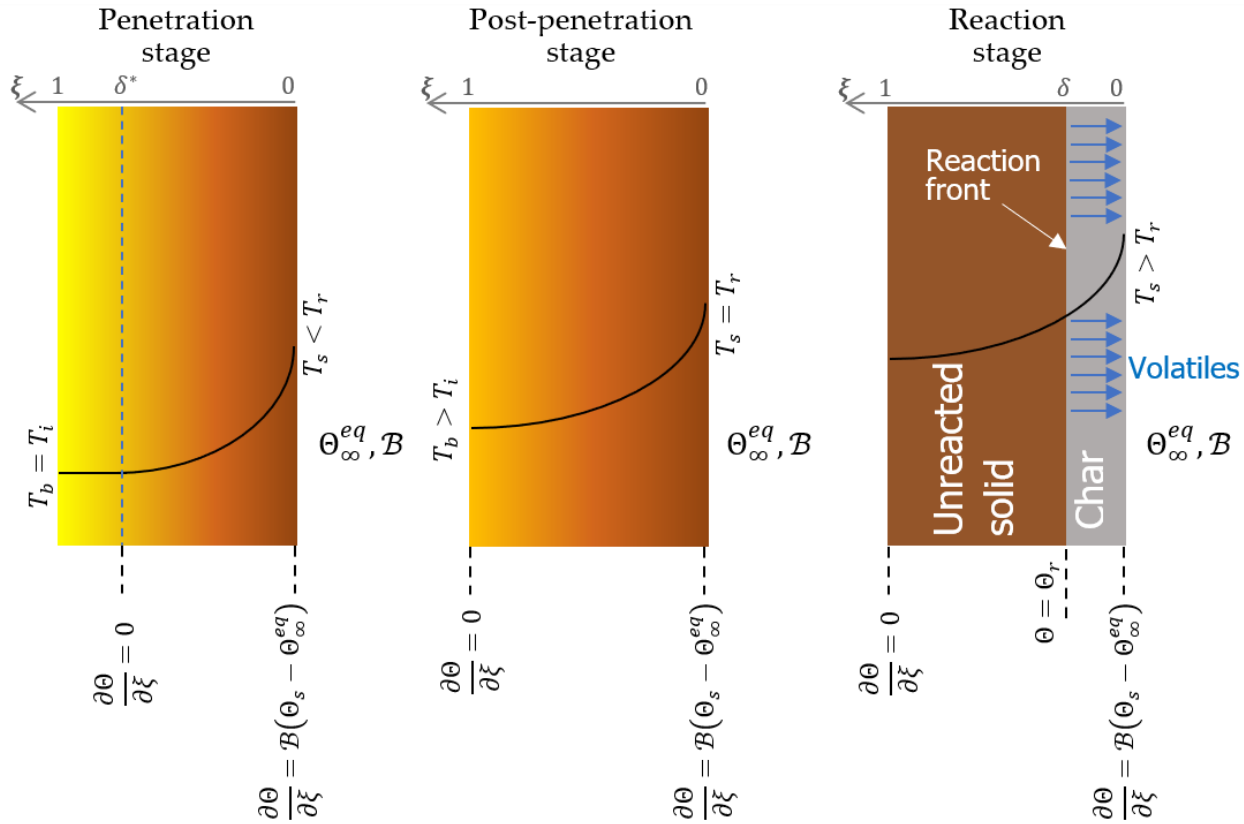

Figure 1. The temperature profile and the boundary conditions at various stages of decomposition of a thermally thin solid particle. $\xi = \delta^*$ denotes the thermal penetration depth and $\xi = \delta$ is the position of the reaction front. T_b and T_s denote back face and surface temperatures, respectively.

As depicted in Figure 1, in the penetration stage, a thermal wave initiated at the particle surface travels toward the adiabatic side of the slab ($\xi = 1$). The post-penetration stage begins as soon as the temperature at the adiabatic side rises above the initial temperature. At this instant, the thermal wave has just reached the adiabatic side of the particle. The transition from the post-penetration to the reaction stage occurs once the surface temperature reaches a characteristic reaction temperature, T_r. A thin reaction front formed at the surface will advance to the interior locations of the solid, leaving a char layer behind, whereas the volatiles will flow toward the surface as depicted in Figure 1. Note that the thermophysical properties will be assumed constant throughout the article.

2.1. Heating Phase

The heat transfer equation in nondimensional form can be written as

$$\frac{\partial \Theta}{\partial \tau} = \frac{\partial^2 \Theta}{\partial \xi^2} \tag{1}$$

where τ ($= \alpha t / L^2$) is a dimensionless time (Fourier number), α is the thermal diffusivity, t is the time, L is the particle thickness, $\xi \in [0,\ 1]$ is a dimensionless position measured from the surface ($\xi = 0$ represents the particle surface), and Θ is a dimensionless temperature defined as

$$\Theta(\xi, \tau) = \frac{T(x,t) - T_\infty}{T_i - T_\infty} \tag{2}$$

where T_i and T_∞ denote the initial temperature of the body and the surrounding temperature, respectively.

During the thermal penetration stage, the initial condition is $\Theta(\xi, 0) = 1$ $(0 \le \xi \le \delta^*)$. The boundary condition at the thermal penetration depth denoted by δ^* may be expressed as $\partial\Theta(\delta^*, \tau)/\partial\xi = 0$. On the other hand, a heat balance at the surface yields another boundary condition as $\partial\Theta(0, \tau)/\partial\xi = \mathcal{B}\left(\Theta_s - \Theta_\infty^{eq}\right)$, where $\mathcal{B}$ denotes a Biot number, $\Theta_s = \Theta(0, \tau)$, and $\Theta_\infty^{eq} = q_{ext}/h(T_i - T_\infty)$ whose value depends on the heat transfer mechanism. For example, $\Theta_\infty^{eq} = 0$ corresponds to a convective heat transfer between the solid and its surroundings. If, on the other hand, the body is heated by external irradiation while losing heat to the surroundings via convection, Θ_∞^{eq} will be nonzero.

Using the initial and boundary conditions defined above and assuming that the spatial temperature distribution approximately follows a quadratic function, a solution of Equation (1) yields [40]

$$\tau = \frac{\delta^{*2}}{12} + \frac{\delta^*}{3\mathcal{B}} - \frac{2}{3\mathcal{B}^2}\ln\left(1 + \frac{\mathcal{B}\delta^*}{2}\right) \tag{3}$$

The temperature profile may then be represented as

$$\Theta = 1 - \left(\frac{1 - \Theta_\infty^{eq}}{1 + \frac{2}{\mathcal{B}\delta^*}}\right)\left(1 - \frac{\xi}{\delta^*}\right)^2 \tag{4}$$

During the post-penetration stage, the adiabatic boundary condition occurs at $\xi = 1$. The surface boundary condition is still the same as described previously for the penetration stage. Further, the initial condition is obtained from Equations (3) and (4) with $\delta^* = 1$. Hence,

$$\tau_t = \frac{1}{12} + \frac{1}{3\mathcal{B}} + \frac{2}{3\mathcal{B}^2}\ln\left(\frac{2}{2 + \mathcal{B}}\right) \tag{5}$$

$$\Theta(\xi, \tau_t) = 1 - \left(\frac{1 - \Theta_\infty^{eq}}{1 + \frac{2}{\mathcal{B}}}\right)(1 - \xi)^2 \tag{6}$$

where τ_t denotes the duration of the penetration stage.

With these initial and boundary conditions, a solution of Equation (1) leads to the following expression for the temperature distribution during the post-penetration stage:

$$\Theta = \Theta_\infty^{eq} + 2\left(\frac{1 - \Theta_\infty^{eq}}{2 + \mathcal{B}}\right)\exp\left[-\frac{3\mathcal{B}}{3 + \mathcal{B}}(\tau - \tau_t)\right]\left(1 + \mathcal{B}\xi - \frac{\mathcal{B}}{2}\xi^2\right) \tag{7}$$

The transition from the post-penetration stage to the reaction stage takes place once $\Theta_s = \Theta_r$. The dimensionless time at which the reaction begins at the surface is determined by substituting $\Theta = \Theta_r$ and ξ = 0 in Equation (7).

$$\tau_r = \tau_t + \frac{3 + \mathcal{B}}{3\mathcal{B}}\ln\left[\left(\frac{2}{2 + \mathcal{B}}\right)\left(\frac{1 - \Theta_\infty^{eq}}{\Theta_r - \Theta_\infty^{eq}}\right)\right] \tag{8}$$

where Θ_r denotes the dimensionless reaction temperature. Indeed, τ_r denotes the total time of the heating stage.

2.2. Reaction Phase

Once the reaction begins at the surface, the body can be divided into two regions:

Charred region $0 \le \xi \le \delta$

Virgin region $\delta \le \xi \le 1$

where δ denotes the dimensionless position of the reaction front.

The conservation of energy in integral form may be represented for the entire solid as

$$\frac{1}{\mathcal{R}}\left(\frac{d}{d\tau}\int_0^{\delta}\Theta d\xi-\Theta_{\mathrm{r}}\frac{d\delta}{d\tau}\right)+\frac{d}{d\tau}\int_{\delta}^{1}\Theta d\xi+\Theta_{\mathrm{r}}\frac{d\delta}{d\tau}=\mathcal{B}\left(\Theta_{\infty}^{eq}-\Theta_s\right)+\mathcal{L}\frac{d\delta}{d\tau}+\mathcal{C}_v(1-\varrho)(\Theta_{\mathrm{r}}-\Theta_s)\frac{d\delta}{d\tau} \tag{9}$$

where $\mathcal{R}=\rho c_p/\rho_c c_{pc}$, $\mathcal{L}=\Delta h_D/c_p(T_i-T_\infty)$, $\mathcal{C}_v=c_{pv}/c_p$, $\varrho=\rho_c/\rho$, the subscript "c" refers to the charred region, Δh_D is the specific enthalpy of the reaction (positive for endothermic and negative for exothermic reaction), and c_{pv} denotes the specific heat of volatiles.

The second and third terms on the right side of Equation (9) account for the heat of solid decomposition and the sensible heat of volatiles, respectively.

The boundary conditions at this stage are $\partial\Theta(0,\tau)/\partial\xi=\kappa\mathcal{B}\left(\Theta_s-\Theta_{\infty}^{eq}\right)$, $\Theta(\delta,\tau)=\Theta_{\mathrm{r}}$, and $\Theta(1,\tau)/\partial\xi=0$, where $\kappa=k^*/k_c^*$ denotes the thermal conductivity ratio.

The temperature profile, assuming a quadratic function satisfying the above boundary conditions, may be expressed as

$$\Theta=\Theta_{\mathrm{r}}+\frac{\kappa\mathcal{B}}{2}\left(\Theta_s-\Theta_{\infty}^{eq}\right)\left[(1-\delta)^2-(1-\xi)^2\right] \tag{10}$$

Using Equation (10) to calculate the integrals in Equation (9) and then integrating with the initial condition $\tau=\tau_r$, $\delta=0$, one obtains

$$\begin{aligned}\frac{\kappa\mathcal{B}}{6\mathcal{R}}\left[\frac{2\delta^3-3\delta^2+2\mathcal{R}(1-\delta)^3}{1+\kappa\mathcal{B}\delta-\frac{\kappa\mathcal{B}}{2}\delta^2}-2\mathcal{R}\right]&=-\frac{\mathcal{B}}{2}\left(\frac{1}{1+\kappa\mathcal{B}\delta-\frac{\kappa\mathcal{B}}{2}\delta^2}+1\right)(\tau-\tau_r)+\frac{\mathcal{L}\delta}{\left(\Theta_{\mathrm{r}}-\Theta_{\infty}^{eq}\right)}\\&+\mathcal{C}_v(1-\varrho)\left\{\delta-\frac{1}{\kappa\mathcal{B}\left(\frac{2}{\kappa\mathcal{B}}+1\right)^{0.5}}\ln\left[\frac{\left(\frac{2}{\kappa\mathcal{B}}+1\right)^{0.5}-1+\delta}{\left(\frac{2}{\kappa\mathcal{B}}+1\right)^{0.5}+1-\delta}\frac{\left(\frac{2}{\kappa\mathcal{B}}+1\right)^{0.5}+1}{\left(\frac{2}{\kappa\mathcal{B}}+1\right)^{0.5}-1}\right]\right\}\end{aligned} \tag{11}$$

The total reaction time can be determined by substituting $\delta=1$ into Equation (11), which upon rearranging gives

$$\begin{aligned}\tau^R&=\tau_r+\left(\frac{4+2\kappa\mathcal{B}}{4+\kappa\mathcal{B}}\right)\left[\frac{\kappa}{3\mathcal{R}}\left(\frac{1}{2+\kappa\mathcal{B}}+\mathcal{R}\right)+\frac{\mathcal{L}}{\mathcal{B}\left(\Theta_{\mathrm{r}}-\Theta_{\infty}^{eq}\right)}\right]\\&+\left(\frac{4+2\kappa\mathcal{B}}{4+\kappa\mathcal{B}}\right)\frac{\mathcal{C}_v}{\mathcal{B}}(1-\varrho)\left\{1-\frac{1}{\kappa\mathcal{B}\left(\frac{2}{\kappa\mathcal{B}}+1\right)^{0.5}}\ln\left[\frac{\left(\frac{2}{\kappa\mathcal{B}}+1\right)^{0.5}+1}{\left(\frac{2}{\kappa\mathcal{B}}+1\right)^{0.5}-1}\right]\right\}\end{aligned} \tag{12}$$

The surface temperature at the end of the reaction may also be estimated using Equation (10). Hence,

$$\Theta_s^R=\frac{2\Theta_{\mathrm{r}}+\kappa\mathcal{B}\Theta_{\infty}^{eq}}{2+\kappa\mathcal{B}} \tag{13}$$

2.3. Validation

The predictability of the formulation presented thus far is examined using the measured data of Lu et al. (2010) who conducted pyrolysis experiments using sawdust particles at a reactor temperature of 1625 K. Table 1 gives the thermophysical properties used in the calculations as well as the predicted and measured total reaction time of single sawdust particles. Heat is transferred to single particles via convection and radiation. So, an equivalent heat transfer coefficient that accounts for both mechanisms has been included in the calculations. The effective thermal conductivity is estimated by accounting for the radiation

in the porous structure of the virgin solid and char as well as the thermal conductivity of the volatiles in the charred region [2,3].

$$k^* = k + 13.5\sigma T^3 \frac{d}{\omega} \tag{14}$$

$$k_c^* = k_c + \varepsilon k_v + 13.5\sigma T^3 \frac{d_c}{\omega} \tag{15}$$

where k is the thermal conductivity of the virgin solid, σ is the Stefan–Boltzmann constant, d is the pore diameter, ω is the emissivity, and k_v is the thermal conductivity of volatiles. Also, ε denotes the porosity of charred region determined as follows:

$$\varepsilon = 1 - (1 - \varepsilon_0)\varrho \tag{16}$$

where ε_0 is the initial or the virgin solid porosity.

Table 1. Thermophysical properties employed in the calculations of sawdust pyrolysis.

Parameter	Quantity	Unit	Source
Thermal conductivity	k = 0.11 k_c = 0.07 k_v = 0.026	W/m·K	[41]
Density	ρ = 650 ρ_c = 33	kg/m^3	
Pore diameter	d_s = 50 d_c = 100	µm	
Porosity	ε_0 = 0.4	-	
Initial temperature	300	K	
Surrounding temperature	1625	K	
Convective heat transfer coefficient	10	W/m^2·K	[35,36]
Reaction time (measured)	0.355	s	[41]
Reaction time (predicted)	0.364	s	Equation (12)

The specific heats of wood, char, and volatiles are calculated using the relations employed in the previous pyrolysis models [2,3]. The heat of the reaction is determined using the correlation of Milosavljevic et al. [42] which accounts for the exothermicity of char formation and the endothermicity of volatile creation.

Figure 2 compares the predicted mass-loss history of the pyrolyzing sawdust particle with the measurements of Lu et al. [41]. A reaction temperature of 589 K is used which was determined by prescribing the measured heating time to Equation (8). The total reaction time predicted by the present formulation is 0.364 s, which compares well with the measured value of 0.355 s. Given the average experimental error of 8.5% reported by Lu et al. [41] and the simplicity of the modeling approach, the validation depicted in Figure 2 is satisfactory.

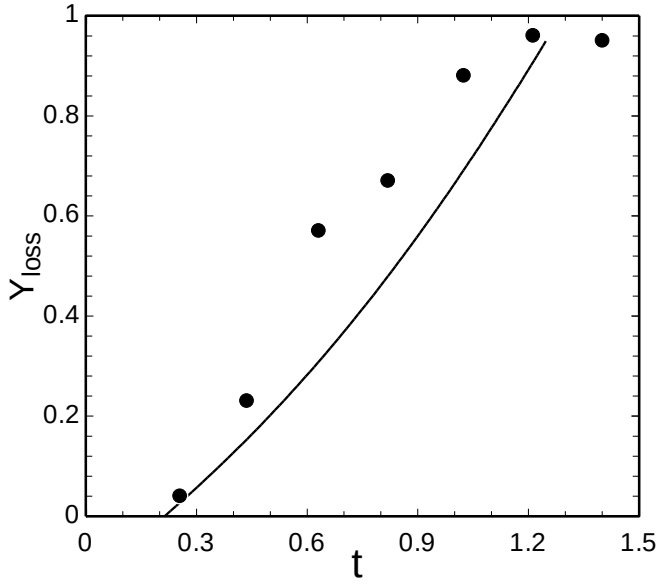

Figure 2. Comparison of the predicted (line) and measured (symbols) mass-loss history of 0.32 mm pyrolyzing sawdust particle. Note that the predicted Y_{loss} is a function of δ where the final mass loss corresponds to $\delta = 1$.

The accuracy of the solid decomposition model is further assessed using the previously developed detailed 1D pyrolysis model [2]. Figure 3 compares the pyrolysis time of spruce and beech particles computed by the present formulation, Equation (12), and the detailed pyrolysis model. The results in Figure 3 are obtained for an external heat flux of 100 kW/m^2. The reaction-front temperature employed in Equation (12) is 700 K. As will be shown in the next section, the reaction front temperature of pyrolyzing wood is dependent on the applied heat flux. The prediction of Equation (12) in Figure 3 qualitatively and quantitatively matches that of the detailed pyrolysis model. Both models predict a longer pyrolysis time for beech than spruce at identical particle sizes as the former (700 kg/m^3) is denser than the latter (450 kg/m^3).

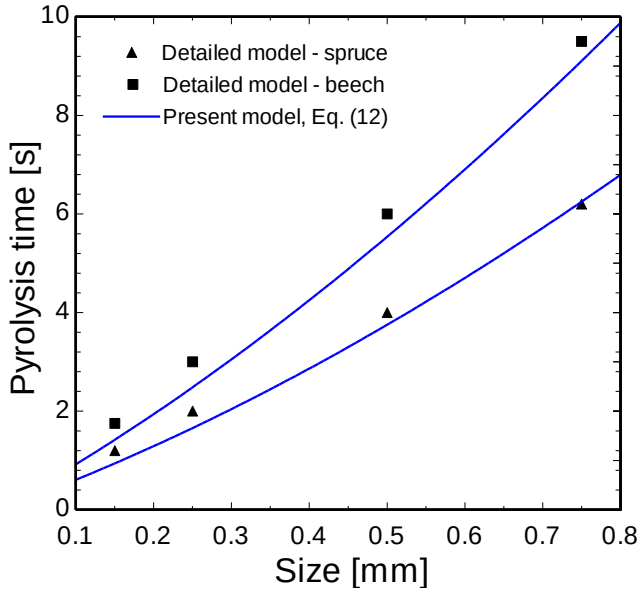

Figure 3. Comparison of the pyrolysis time of spruce and beech particles predicted by Equation (12) and a detailed pyrolysis model [2] at varying particle size and an external heat flux of 100 kW/m^2. A reaction-front temperature of 700 K is employed in Equation (12). The pyrolysis time computed by the detailed model can also be found in Ref. [43].

3. Determination of Pyrolysis-Front Temperature

Now, the question is how one may determine the reaction temperature in the absence of experimental data. The method employed for the calculation of the average volumetric pyrolysis-front temperature includes the incorporation of a correlation between the external heat flux and pyrolysis time. Elimination of the pyrolysis time between the correlation and Equation (12) will allow to express the pyrolysis-front temperature as a function of the external heat flux. A typical trend of the total pyrolysis time of single wood particles versus external heat flux is depicted in Figure 4. The results shown in Figure 4 are obtained from Haseli et al. [2], whose model accounts for the solid decomposition in accordance with the kinetic scheme of Shafizadeh and Chin [44]. The model is based upon the conservation of species mass (biomass, gases, tar, char), energy, and gas-phase momentum and has been validated using experiments.

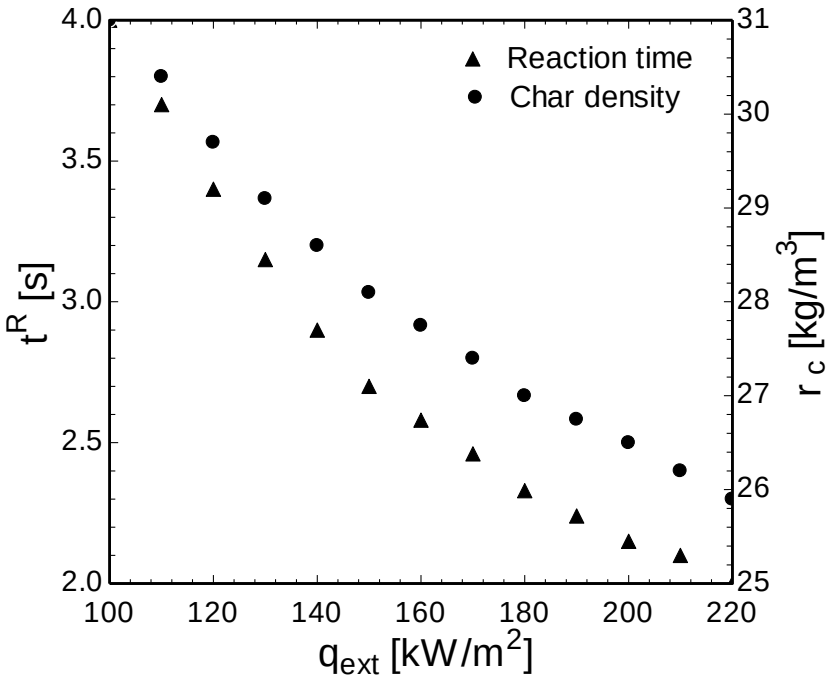

Figure 4. Char density and reaction time of pyrolyzing spruce particles predicted by a detailed pyrolysis model [2]. Particle size: 1 mm.

Of primary importance is the functional relation of the reaction time t^R with the external heat flux q_{ext}. Both the final char density and reaction time of pyrolyzing wood particles exhibit descending trends with the external heat flux. This observation will suffice for the development of an analytical model for the pyrolysis-front temperature in the next section. First, we numerically demonstrate the method described above to determine the pyrolysis-front temperature of the wood particles of Figure 4 at different heat fluxes using the properties given in Table 2. It is to be noted that in practice the reaction temperature is expected to vary within the particle. So, the pyrolysis-front temperature to be obtained using the proposed method may be treated as a volumetric average quantity.

Table 2. Properties of dry spruce wood [45].

Property	Quantity	Unit
Thermal conductivity	0.35	W/m·K
Density	450	kg/m^3
Surface emissivity	0.9	-
Initial temperature	300	K
Surrounding temperature	400	K

Figure 5 shows the computed average pyrolysis-front temperature for spruce wood at varying irradiation heat flux in both dimensional (5a) and dimensionless (5b) formats. The noticeable observation is that the pyrolysis-front temperature (i) is dependent on the applied heat flux and (ii) has an extremum at an external heat flux of 91.5 kW/m^2 (equivalent to $\Theta_{\infty}^{eq} = -26.7$). The pyrolysis-front temperature increases from 545.6 K to 705.4 K with an increase in the external heat flux for $q_{ext} < 91.5$ kW/m^2 ($\Theta_{\infty}^{eq} < -26.7$), but it decreases with a further increase in q_{ext} beyond the optimum heat flux, i.e., 91.5 kW/m^2.

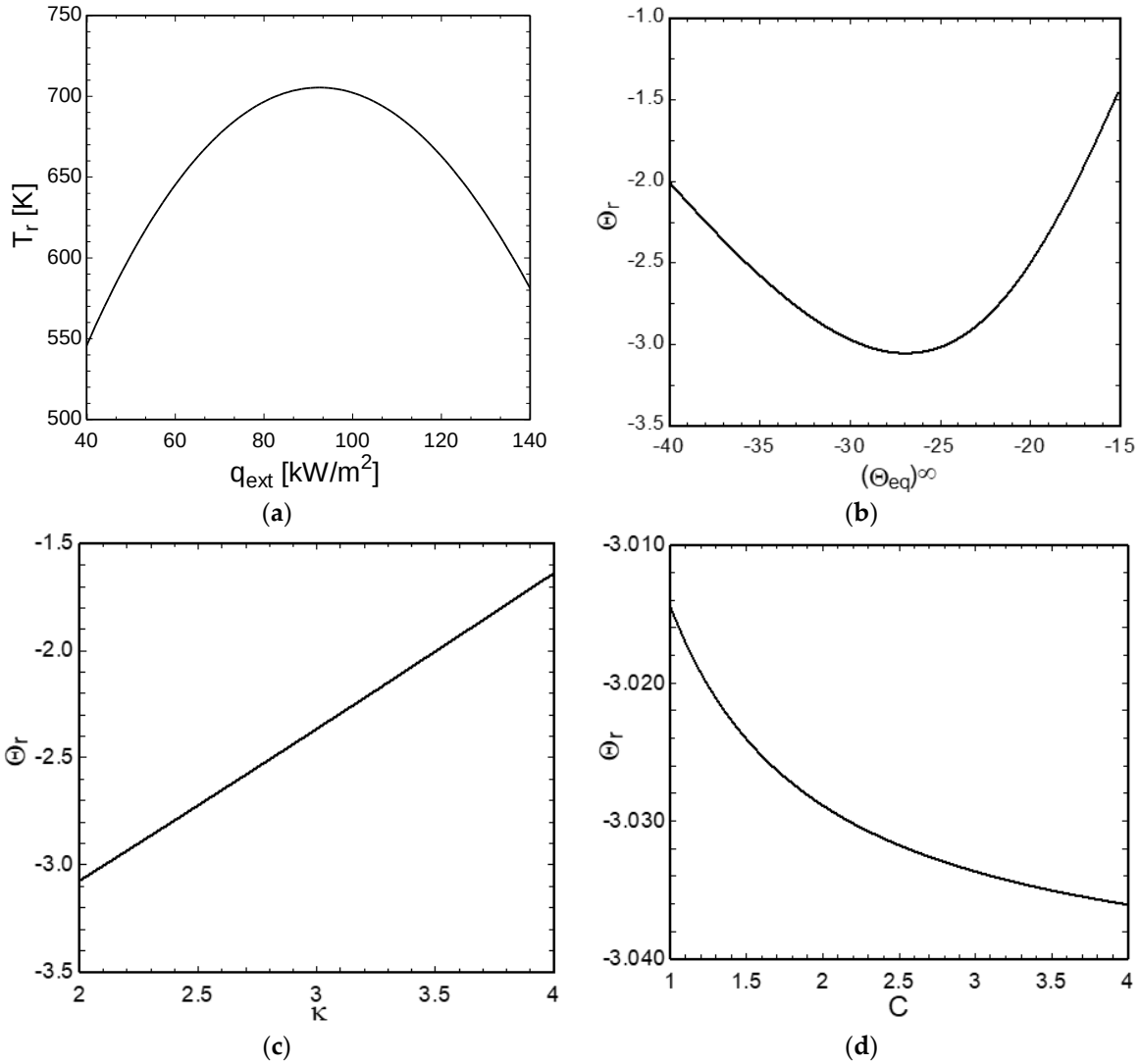

Figure 5. Pyrolysis-front temperature of single spruce particles obtained from the combination of the published results [2] and the present model. (**a**) Reaction temperature vs. external heat flux; (**b**) dimensionless reaction temperature vs. dimensionless heat flux. (**c**,**d**) Dimensionless reaction front temperature varying with thermal conductivity ratio ($\mathcal{K}$) and specific heat ratio ($\mathcal{C} = c_p/c_{pc}$) at an external heat flux of 80 kW/m^2.

Park et al. [25] investigated the effect of external heat flux that ranged from 20 to 100 kW/m^2. They found that the pyrolysis-front temperature increased with an increase in the heat flux; this trend is consistent with the results shown in Figure 5a where the pyrolysis-front temperature exhibits an increasing trend up to a heat flux of close to 100 kW/m^2. The authors noted that with a further increase in the heat flux, an asymptotic value could be reached for the pyrolysis-front temperature. This asymptotic temperature value occurring at the vicinity of 100 kW/m^2 external heat flux is coincident with the location of the maximum reaction temperature in Figure 5a.

By inspecting Equations (8) and (12), it can be readily inferred that the total reaction time, τ^R, is dependent on the external heat flux through $\ln\left[\left(1-\Theta_\infty^{eq}\right)/\left(\Theta_\mathrm{r}-\Theta_\infty^{eq}\right)\right]$ and $1/\left(\Theta_\mathrm{r}-\Theta_\infty^{eq}\right)$. Both terms are decreasing functions with respect to the external heat flux but increasing with the reaction temperature. The former (the *ln* term) influences the time of the heating stage, whereas the latter impacts the time of the pyrolysis stage. The comprehensive pyrolysis model [2,3] considers finite-rate temperature-dependent decomposition of biomass through three parallel reaction pathways in that biomass is converted into char, tar, and gas. In the present formulation, all these effects are included in the characteristic reaction temperature Θ_r.

The total pyrolysis time predicted by Equation (12) is constrained to match that of the comprehensive model. Any difference between the times predicted by the two models is offset through the characteristic reaction-front temperature. At low heat fluxes, the slopes of both $\ln\left[\left(1-\Theta_\infty^{eq}\right)/\left(\Theta_\mathrm{r}-\Theta_\infty^{eq}\right)\right]$ and $1/\left(\Theta_\mathrm{r}-\Theta_\infty^{eq}\right)$ are steep, and these slopes gradually decrease with an increase in the heat flux. Equation (12) that includes the above two terms appears to predict a shorter time at low heat fluxes but a longer time at high heat fluxes compared to the comprehensive pyrolysis model. This is why the reaction-front temperature increases with an increase in q_{ext} at low heat fluxes but decreases at high heat fluxes, indicating that there exists a q_{ext} between the two regions of low and high heat fluxes at which the pyrolysis temperature attains a maximum. From the above discussion, the pyrolysis temperature in the simplified particle models developed based on thin reaction-front approximation and an infinite reaction rate can be viewed as a fitting parameter.

The effect of the thermal conductivity ratio κ and the specific heat ratio $\mathcal{C}$ $(= c_p/c_{pc})$ on the reaction-front temperature is depicted in Figure 5c,d, respectively. The specific heat ratio marginally impacts Θ_r but it is noticeably sensitive to a change in the thermal conductivity ratio. An increase in the specific heat ratio leads to a slight reduction in Θ_r equivalent to a marginal increase in T_r. On the contrary, an increase in the thermal conductivity ratio yields a higher Θ_r (lower T_r). These trends are consistent with the findings of Park et al. [25], who reported that the pyrolysis temperature would slightly decrease with a 2.5-fold increase in the char specific heat and slightly increase with a 2-fold increase in the virgin solid specific heat. The authors also found an increase in the pyrolysis temperature (equivalent to a decrease in Θ_r) when the thermal conductivity of char was increased (equivalent to decreasing κ). In the next section, the existence of an extremum reaction temperature will analytically be examined.

4. Formulation of Pyrolysis-Front Temperature

To obtain an expression for Θ_r, the reaction time and char density predicted by the detailed pyrolysis model are algebraically incorporated into Equation (12). Because the formulation in Section 2 is presented in a dimensionless form, it is appropriate to describe the reaction time, char density, and heat flux using the dimensionless notations, i.e., $\varrho = \mathcal{F}\left(\Theta_\infty^{eq}\right)$ and $\tau^R = \mathcal{G}\left(\Theta_\infty^{eq}\right)$. One may choose various functions, e.g., polynomial, exponential, and linear, for $\mathcal{F}$ and $\mathcal{G}$ to fit the prediction of the detailed model with sufficient accuracy. It should, however, be noted that the complexity of the formulation to be presented below strictly depends on the type of function assigned to $\mathcal{F}$ and $\mathcal{G}$. Among numerous possibilities, a linear function is found to ensure the simplicity of the formulation without relinquishing the accuracy (R^2-value greater than 0.96 for both $\mathcal{F}$ and $\mathcal{G}$).

$$\varrho = \beta_1 \Theta_\infty^{eq} + \beta_0 \tag{17}$$

$$\tau^R = \gamma_1 \Theta_\infty^{eq} + \gamma_0 \tag{18}$$

where γ_0, γ_1, β_0, and β_1 are constant parameters.

Noting that $\left(1+\frac{\mathcal{B}}{2}\right)\left(\frac{\Theta_{\mathrm{r}}-\Theta_{\infty}^{eq}}{1-\Theta_{\infty}^{eq}}\right)\approx 1$, Equation (8) may be rewritten using Equation (5) as

$$\tau_r = \frac{1}{12} - \frac{2+\mathcal{B}}{3\mathcal{B}} + \frac{2}{3\mathcal{B}^2}\ln\left(\frac{2}{2+\mathcal{B}}\right) + \frac{3+\mathcal{B}}{3\mathcal{B}}\left(\frac{2}{2+\mathcal{B}}\right)\left(\frac{1-\Theta_{\infty}^{eq}}{\Theta_{\mathrm{r}}-\Theta_{\infty}^{eq}}\right) \tag{19}$$

Substituting Equations (17)–(19) into Equation (12) and rearranging for Θ_{r} yields

$$\Theta_{\mathrm{r}} = \Theta_{\infty}^{eq} + \frac{\mathfrak{B}_2\left(1-\Theta_{\infty}^{eq}\right)+\mathfrak{B}_4}{\mathfrak{B}_1+\mathfrak{B}_3\Theta_{\infty}^{eq}} \tag{20}$$

where

$$\begin{aligned}\mathfrak{B}_1 = {} & \gamma_0 - \tfrac{1}{12} + \tfrac{2+\mathcal{B}}{3\mathcal{B}} - \tfrac{2}{3\mathcal{B}^2}\ln\left(\tfrac{2}{2+\mathcal{B}}\right) - \left(\tfrac{1}{4+\hbar\mathcal{B}}\right)\tfrac{2\hbar}{3}\left(2+\hbar\mathcal{B}+\tfrac{\beta_0}{\mathcal{C}}\right) \\ & +(\beta_0-1)\tfrac{\mathcal{C}_v}{\mathcal{B}}\left(\tfrac{4+2\hbar\mathcal{B}}{4+\hbar\mathcal{B}}\right)\left\{1-\frac{1}{\hbar\mathcal{B}\left(\frac{2}{\hbar\mathcal{B}}+1\right)^{0.5}}\ln\left[\frac{\left(\frac{2}{\hbar\mathcal{B}}+1\right)^{0.5}+1}{\left(\frac{2}{\hbar\mathcal{B}}+1\right)^{0.5}-1}\right]\right\}\end{aligned} \tag{21}$$

$$\mathfrak{B}_2 = \frac{3+\mathcal{B}}{3\mathcal{B}}\left(\frac{2}{2+\mathcal{B}}\right) \tag{22}$$

$$\mathfrak{B}_3 = \gamma_1 - \frac{2\beta_1}{3\mathcal{C}}\left(\frac{\hbar}{4+\hbar\mathcal{B}}\right) + \beta_1\left(\frac{4+2\hbar\mathcal{B}}{4+\hbar\mathcal{B}}\right)\frac{\mathcal{C}_v}{\mathcal{B}}\left\{1-\frac{1}{\hbar\mathcal{B}\left(\frac{2}{\hbar\mathcal{B}}+1\right)^{0.5}}\ln\left[\frac{\left(\frac{2}{\hbar\mathcal{B}}+1\right)^{0.5}+1}{\left(\frac{2}{\hbar\mathcal{B}}+1\right)^{0.5}-1}\right]\right\} \tag{23}$$

$$\mathfrak{B}_4 = \left(\frac{4+2\hbar\mathcal{B}}{4+\hbar\mathcal{B}}\right)\frac{\mathcal{L}}{\mathcal{B}} \tag{24}$$

The above analysis reveals that Θ_{r} is a function of Θ_{∞}^{eq}, the Biot number $\mathcal{B}$, the thermal conductivity ratio $\hbar$, the specific heat ratios $\mathcal{C}$ and $\mathcal{C}_v$, and $\mathcal{L}$. Equating the differential of Θ_{r} with respect to Θ_{∞}^{eq} to zero, $\left(\partial\Theta_{\mathrm{r}}/\partial\Theta_{\infty}^{eq}\right)=0$, and solving for Θ_{∞}^{eq} leads to

$$\left(\Theta_{\infty}^{eq}\right)^{*} = \frac{1}{\mathfrak{B}_3}\left\{\left(\mathfrak{B}_1\mathfrak{B}_2+\mathfrak{B}_2\mathfrak{B}_3+\mathfrak{B}_3\mathfrak{B}_4\right)^{\frac{1}{2}}-\mathfrak{B}_1\right\} \tag{25}$$

With an increase in Θ_{∞}^{eq}, Θ_{r} will decrease if $\Theta_{\infty}^{eq} < \left(\Theta_{\infty}^{eq}\right)^{*}$, but it will increase if $\Theta_{\infty}^{eq} > \left(\Theta_{\infty}^{eq}\right)^{*}$. The dimensionless reaction temperature corresponding to $\left(\Theta_{\infty}^{eq}\right)^{*}$ may be determined by substituting Equation (25) into Equation (20) and simplifying as

$$\Theta_{\mathrm{r}}^{*} = \frac{1}{\mathfrak{B}_3}\left[2\left(\mathfrak{B}_1\mathfrak{B}_2+\mathfrak{B}_2\mathfrak{B}_3+\mathfrak{B}_3\mathfrak{B}_4\right)^{\frac{1}{2}}-\left(\mathfrak{B}_1+\mathfrak{B}_2\right)\right] \tag{26}$$

A relation may also be established between Θ_{r}^{*} and $\left(\Theta_{\infty}^{eq}\right)^{*}$ through a combination of Equations (25) and (26) as follows:

$$\Theta_{\mathrm{r}}^{*} = 2\left(\Theta_{\infty}^{eq}\right)^{*} + \frac{\mathfrak{B}_1-\mathfrak{B}_2}{\mathfrak{B}_3} \tag{27}$$

As an example, we determine the extremum reaction temperature of the pyrolyzing spruce particle using the properties given in Table 2. At the condition of extremum temperature, we have the following values for the dimensionless parameters:

$$\mathcal{B}=0.048,\ \hbar=2.64,\ \mathcal{C}_v=0.847,\ \mathcal{C}=1.26,\ \mathcal{L}=1.99$$

Using the above quantities in Equations (21)–(24), we obtain

$$\mathfrak{B}_1 = 32.16,\ \mathfrak{B}_2 = 20.67,\ \mathfrak{B}_3 = 0.2275,\ \mathfrak{B}_4 = 42.73$$

Substituting these values into Equations (25) and (27) yields $\left(\Theta_\infty^{eq}\right)^* = -26.81$ and $\Theta_r^* = -3.11$. So, the dimensionless reaction front temperature should decrease with Θ_∞^{eq} for $\Theta_\infty^{eq} < -26.81$ and increase if $\Theta_\infty^{eq} > -26.81$. These observations are consistent with the trend of Θ_r vs. Θ_∞^{eq} in Figure 5b. Furthermore, the dimensional values of the extremum pyrolysis temperature and the optimum heat flux at $\left(\Theta_\infty^{eq}\right)^*$ are determined to be 711.3 K and 88.5 kW/m^2, respectively which compare fairly with the maximum pyrolysis temperature of 705.4 K and the optimum heat flux of 91.5 kW/m^2 in Figure 5a.

5. Formulation of Ignition Temperature

The expression given by Equation (20) provides an estimate of the average reaction-front temperature throughout the particle over the conversion time, which is not necessarily the same as the ignition temperature [46]. One may find various terminologies in the literature for the ignition temperature of a reacting solid, for instance, piloted ignition that requires the presence of a spark ignitor, or auto-ignition where the volatile temperature rises to auto-ignition level [30]. Past studies [27,32,37,47–50] have revealed a dependency of the ignition temperature on irradiation heat flux. In some cases, extremum ignition temperatures have been observed.

Quintiere and co-workers [27,48,49] experimentally studied the ignition of wood species at an external heat flux that varied between 10 and 75 kW/m^2. An interesting trend that one may notice in the work of Quintiere et al. is that the glowing ignition temperature plotted against the external heat flux exhibits a hat-like (~) shape with two distinct local extremums—see Figure 5 in the work of Spearpoint and Quintiere [27] and Figure 5b in the work of Boonmee and Quintiere [48]. The ignition temperature rapidly rises between 10 kW/m^2 and around 20 kW/m^2 where the first extremum is noticeable. It then decreases down to the second extremum, beyond which it begins to take off. On the contrary, the flaming ignition decreases monotonically with the incident heat flux.

McAllister and Finney [50], who experimented the autoignition of red oak cylinders and disks, have reported similar findings. The ignition temperature plotted against the heat flux exhibited a hat-like trend for red oak disks, whereas the ignition temperature of rods decreased with an increase in the heat flux. The authors observed rare signs of smoldering for the disk and significant smoldering with gas-phase ignition for the rods. The hat-shape phenomenon can also be observed in the autoignition data of PMMA measured by Kashiwagi [33] for a high heat flux varying between 100 and 200 kW/m^2; see figure 23 in Ref. [33]. Kashiwagi also measured the ignition temperature for red oak and found a decreasing trend with the applied external heat flux. As noted by the author, the red oak ignition at high heat fluxes was due to the volatiles' ignition.

From the above discussion, the regime of ignition depends on whether the gases released due to the solid decomposition have reached an ignition temperature. The hat-shape phenomenon seems to occur in the absence of gas-phase ignition. To prove this mathematically, a relation will be derived between the ignition temperature and the external heat flux that can explain the above observations using a similar method described in the previous section which led to an expression for the reaction-front temperature, i.e., Equation (20).

Since experimental studies commonly measure time-to-ignition at a given external heat flux [26,27,47–50], such measurements may be integrated with the expression obtained from the formulation described in Section 2.1, i.e., Equation (8). This treatment allows for eliminating the time-to-ignition, t_{ig}, and establishing an explicit relation between the ignition temperature and the external heat flux. The measured t_{ig} vs. q_{ext} data may best be fitted by a power function. An example is shown in Figure 6 which plots the measured

ignition data of wood and PMMA extracted from [48,49,51]. The trendline fitting the data obeys

$$t_{ig} = \frac{C_0}{q_{ext}^n} \tag{28}$$

where C_0 is a correlation constant that is material-dependent, and n is an exponent coefficient (n = 2 for the PMMA and n = 3 for the wood).

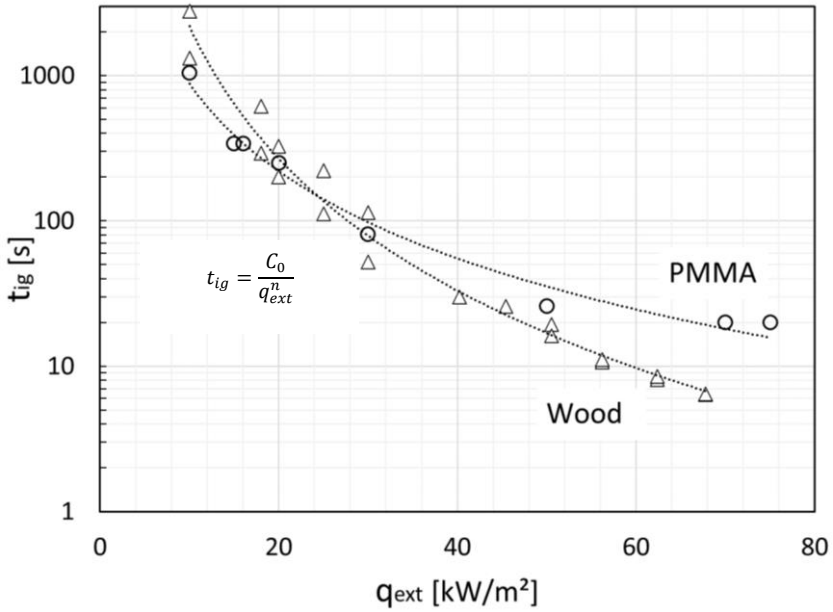

Figure 6. Typical measured time-to-ignition data of PMMA (circles) and wood (triangles) against the applied external heat flux and the power-law trendline fitting the data. $C_0 = 836.8(10^8)$ W^2·s/m^2 and n = 2 for PMMA; $C_0 = 20.0(10^{14})$ W^3·s/m^3 and n = 3 for wood. Data are extracted from [48,49] for wood and [51] for PMMA.

To incorporate Equation (28) into Equation (8), it would then be unsuitable to use the dimensionless temperature defined in Equation (2), so both the reaction temperature and heat flux in Equation (8) are presented in a normalized form. Thus,

$$\tau_{ig} = \tau_t + \frac{3+\mathcal{B}}{3\mathcal{B}} \ln\left[\left(\frac{2}{2+\mathcal{B}}\right)\left(\frac{1-\theta_\infty-\phi}{\theta_{ig}-\theta_\infty-\phi}\right)\right] \tag{29}$$

where $\theta_{ig} = T_{ig}/T_i$, $\theta_\infty = T_\infty/T_i$, and $\phi = (q_{ext}/hT_i)$.

Substituting Equations (5) and (28) into Equation (29) and rearranging for θ_{ig} yields

$$\theta_{ig} = \theta_\infty + \phi + (1-\theta_\infty-\phi)\mathfrak{D}_1 \exp\left(-\frac{3}{3\mathcal{B}+\mathcal{B}^2}\frac{\mathfrak{D}_0}{\phi^n}\right) \tag{30}$$

where

$$\mathfrak{D}_0 = \frac{C_0}{k\rho c_p}\frac{1}{(T_i)^n h^{n-2}} \tag{31}$$

$$\mathfrak{D}_1 = \exp\left\{\left(\frac{1}{3+\mathcal{B}}\right)\left[1+\frac{\mathcal{B}}{4}+\frac{2+3\mathcal{B}+\mathcal{B}^2}{\mathcal{B}}\ln\left(\frac{2}{2+\mathcal{B}}\right)\right]\right\} \tag{32}$$

Equation (30) states that the normalized ignition temperature is a function of ϕ, $\mathcal{B}$, and the dimensionless parameter $\mathfrak{D}_0$ that depends on the thermophysical properties. It is to

be noted that Equation (30) is obtained assuming that the solid will remain inert until the ignition. For identical initial and surrounding temperatures, $\theta_\infty = 1$, we have

$$\theta_{ig} = 1 + \phi\left[1 - \mathfrak{D}_1 \exp\left(-\frac{3}{3\mathcal{B} + \mathcal{B}^2}\frac{\mathfrak{D}_0}{\phi^n}\right)\right] \tag{33}$$

Figure 7 shows the predicted ignition temperature for wood and PMMA. The hat-like (~) trend is qualitatively the same as that observed in past studies [27,33,48–50]. The ignition temperature possesses a maximum value at a low heat flux. It then decreases gradually with a further increase in the heat flux and attains a local minimum at a high heat flux. For the PMMA, the extremum temperatures in Figure 7 are $\theta_{ig} = 2.18$ and 2.06 that occur at $\phi = 1.79$ and 4.89, respectively. For the wood, the local maximum and minimum temperatures are $\theta_{ig} = 2.47$ and 2.26 that take place at $\phi = 1.78$ and 4.61, respectively. Note that the ignition temperatures are higher for wood than for PMMA at identical normalized heat fluxes, an observation that is consistent with the experimental observations of Kashiwagi [31,32].

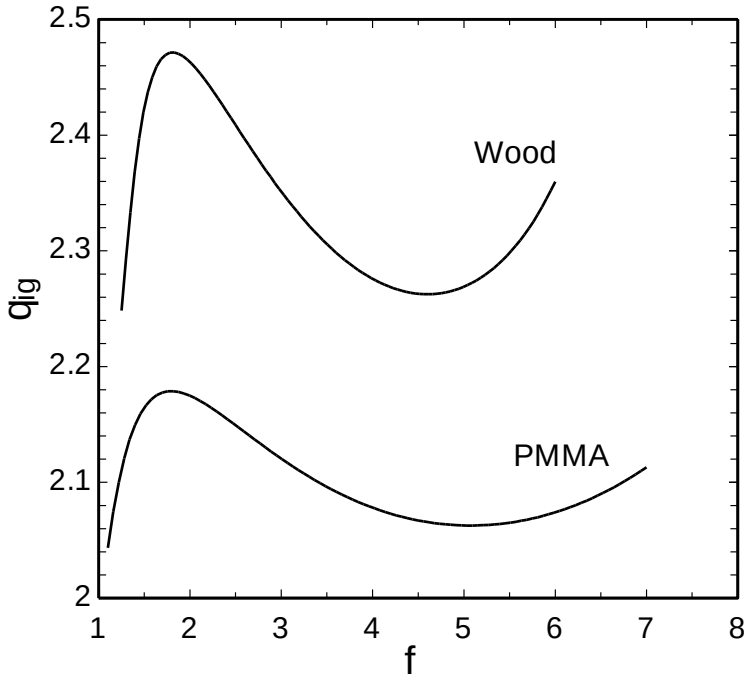

Figure 7. Comparison of the predicted ignition temperatures for wood and PMMA.

At high heat fluxes, the *exp* term in Equation (33) is sufficiently small, so one may apply the relation $\exp(-y) \approx 1 - y$ (valid for $y \to 0$) and rewrite it as follows:

$$\theta_{ig} = 1 + (1 - \mathfrak{D}_1)\phi + \frac{3}{3\mathcal{B} + \mathcal{B}^2}\frac{\mathfrak{D}_1\mathfrak{D}_0}{\phi^{n-1}} \tag{34}$$

Solving $\partial\theta_{ig}/\partial\phi = 0$ leads to

$$\phi^* = \left[\frac{3(n-1)}{3\mathcal{B} + \mathcal{B}^2}\left(\frac{\mathfrak{D}_1\mathfrak{D}_0}{1 - \mathfrak{D}_1}\right)\right]^{\frac{1}{n}} \tag{35}$$

Equation (35) provides an estimation of the normalized heat flux at the second extremum temperature (the local minimum). Calculating the second derivative of θ_{ig} at ϕ^* yields

$$\left(\frac{\partial^2\theta_{ig}}{\partial\phi^2}\right)_{\phi^*} = n(1-\mathfrak{D}_1)^{\frac{n+1}{n}}\left[\frac{3\mathcal{B}+\mathcal{B}^2}{3(n-1)\mathfrak{D}_1\mathfrak{D}_0}\right]^{\frac{1}{n}} \tag{36}$$

where $\mathcal{B} > 0$, $\mathfrak{D}_0 > 0$, and $n > 1$. Parameter $\mathfrak{D}_1$ defined in Equation (32) is a decreasing function of $\mathcal{B}$ as depicted in Figure 8 which shows that $0 < \mathfrak{D}_1 < 1$. It can be inferred from Equation (32) that for $\mathcal{B}$ approaching 0, $\mathfrak{D}_1 \to 1$. It may then be concluded that the right side of Equation (36) is positive; that is, the heat flux given in Equation (35) is a local minimum.

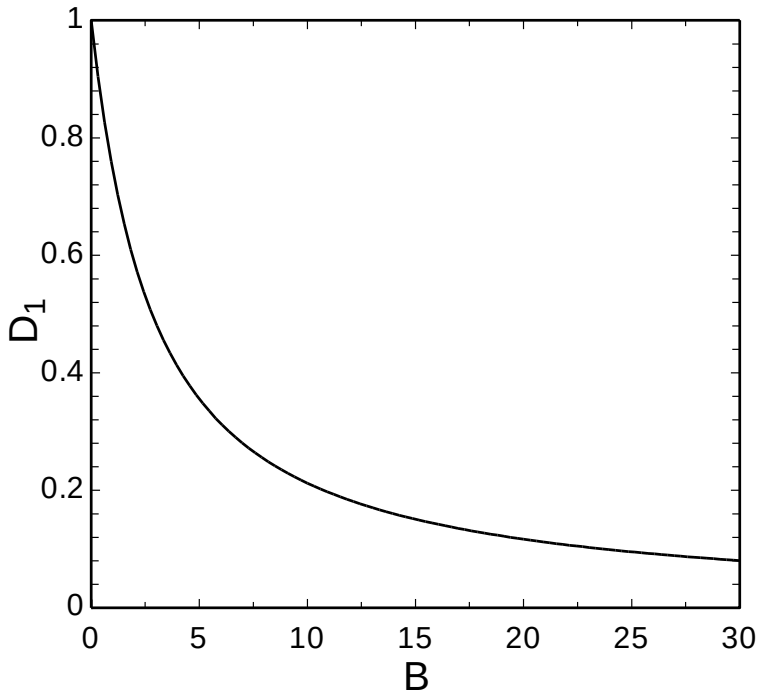

Figure 8. The graphical dependence of parameter $\mathfrak{D}_1$ on the Biot number.

Substituting Equation (35) into Equation (34), we find

$$\theta^*_{ig} = 1 + n\left(\frac{n-1}{1-\mathfrak{D}_1}\right)^{\frac{1-n}{n}}\left(\frac{3\mathfrak{D}_1\mathfrak{D}_0}{3\mathcal{B}+\mathcal{B}^2}\right)^{\frac{1}{n}} \tag{37}$$

On the other hand, a combination of Equations (35) and (37) allows to establish a relation between θ^*_{ig} and ϕ^* at the local minimum.

$$\theta^*_{ig} = 1 + \left(\frac{n}{n-1}\right)(1-\mathfrak{D}_1)\phi^* \tag{38}$$

Equation (38) states that the ignition temperature at the local minimum will be higher if the corresponding optimum heat flux is higher. For PMMA with the Biot number of 0.325 [51], we have $\mathfrak{D}_0 = 1.208$ and $\mathfrak{D}_1 = 0.901$, which upon substitution in Equations (35) and (38) yield $\phi^* = 5.53$ and $\theta^*_{ig} = 2.09$. These figures are reasonably close to the normalized ignition temperature of 2.06 and the normalized heat flux of 4.89 at the location of the second extremum in Figure 7. On the other hand, for wood, the Biot number is 0.631, so $\mathfrak{D}_0 = 6.089$ and $\mathfrak{D}_1 = 823$. The optimum heat flux and the local minimum ignition

temperature obtained from Equations (35) and (38) are $\phi^* = 4.66$ and $\theta_{ig}^* = 2.24$, which compare well with the respective quantities $\theta_{ig}^* = 2.26$ and $\phi^* = 4.61$ in Figure 7.

To examine the effect of the Biot number and the new property $\mathfrak{D}_0$, Equation (33) is used to produce θ_{ig} vs. ϕ profiles at different values of $\mathcal{B}$ and $\mathfrak{D}_0$. The results are depicted in Figure 9. As the Biot number increases, both extremums occur at a lower heat flux, whereas the first extremum temperature decreases but that of the second extremum (the local minimum) increases. For low heat fluxes $\phi \leq 4$, the ignition temperature is lower at a higher Biot number. However, this trend is opposite at high heat fluxes $\phi \geq 7$ where the ignition temperature may rise with an increase in the Biot number. On the other hand, the ignition temperature is predicted to increase with an increase in $\mathfrak{D}_0$ nearly uniformly over the range of ϕ shown in Figure 9. Both extremums shift toward a higher heat flux at a greater $\mathfrak{D}_0$, and the temperature plateau discussed previously is visible in all cases.

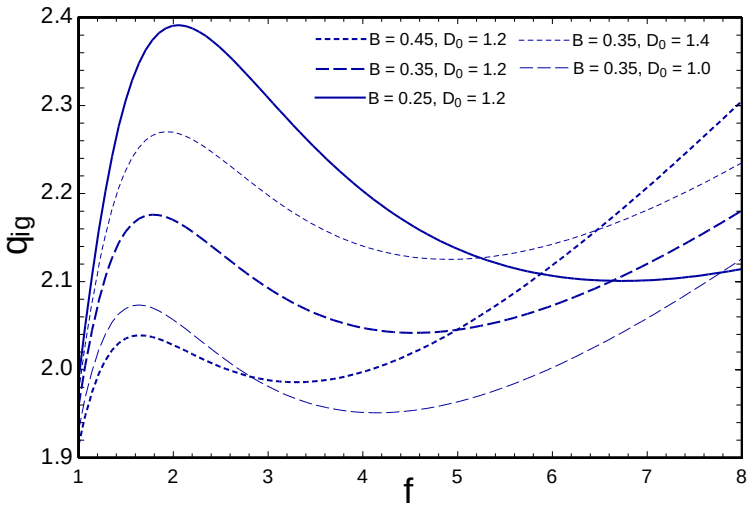

Figure 9. The effect of Biot number and the dimensionless parameter $\mathfrak{D}_0$ on the ignition temperature ($n = 2$).

6. Conclusions

This work investigated the reaction-front and ignition temperatures of thermally decomposing solids by means of analytical formulation. The method includes eliminating time by incorporating a correlation between the process time and applied external heat flux. Explicit expressions were derived for the pyrolysis-front and ignition temperatures, i.e., Equations (20) and (33), as well as the extremum temperatures, i.e., Equations (26) and (37), as a function of the external heat flux and Biot number. The results show that the pyrolysis-front temperature also depends noticeably on the thermal conductivity ratio ($\mathcal{k}$), whereas the ignition temperature is found to be dependent on a new property, $\mathfrak{D}_0$, defined in Equation (31). The pyrolysis-front temperature is found to possess a maximum at an external heat flux of 91.5 kW/m^2. On the other hand, the ignition temperature exhibits a local maximum at a low heat flux and a local minimum at a higher heat flux—the hat-like trend. These extremum ignition temperatures have experimentally been observed in some past studies where ignition occurred in the absence of the gas-phase reaction. It may be concluded that the hat-like phenomenon represents an ignition mode in that no or negligible volatile oxidation takes place. Including solid and volatile combustion in the ignition model could help explain other ignition modes. Further experimental studies are needed to examine the proposed method over a wider range of external heat fluxes and solid materials.

Funding: This research received no external funding.

Data Availability Statement: Data will be made available on request.

Conflicts of Interest: The author declares there are no competing interests.

Nomenclature

$\mathfrak{B}_1, \ldots, \mathfrak{B}_4$	Coefficients of Equation (20)
$\mathcal{B}$	Biot number
$\mathcal{C}$	Specific heat ratio ($= c_p/c_{pc}$)
$\mathcal{C}_v$	$= c_{pv}/c_p$
C_0	Correlation constant in Equation (35), $W^2 \cdot s/m^2$
c_p	Specific heat, J/kg·K
$\mathfrak{D}_0, \mathfrak{D}_1$	Dimensionless parameters in Equation (30)
d	Pore diameter, m
h	Heat transfer coefficient, $W/m^2 \cdot K$
k	Thermal conductivity, W/m·K
$\hbar$	Thermal conductivity ratio ($= k^*/k_c^*$)
k^*	Effective thermal conductivity, W/m·K
$\mathcal{L}$	Dimensionless reaction enthalpy ($= \Delta h_D/c_p(T_i - T_\infty)$)
n	Correlation coefficient, Equation (36)
q_{ext}	External heat flux, W/m^2
$\mathcal{R}$	Heat capacity ratio ($\rho c_p/\rho_c c_{pc}$)
T	Temperature, K
t	Time, sec
x	Position, m
Greek Letters	
δ	Dimensionless reaction front depth
δ^*	Dimensionless thermal penetration depth
ε	Porosity of char
θ	Normalized temperature ($= T/T_i$)
Θ	Dimensionless temperature defined in Equation (2)
Θ_∞^{eq}	$= \frac{q_{ext}}{h(T_i - T_\infty)}$
ξ	Dimensionless position
ρ	Solid density, kg/m^3
ϱ	Density ratio ($= \rho_c/\rho$)
σ	Stefan–Boltzmann constant
τ	Dimensionless time ($= \alpha t/L^2$)
τ^R	Dimensionless reaction time
ϕ	Normalized heat flux ($= q_{ext}/hT_i$)
ω	Emissivity
Subscripts	
∞	Surrounding
c	Char
i	Initial
ig	Ignition
r	Reaction
s	Surface
v	Volatiles

References

1. Park, W.C.; Atreya, A.; Baum, H.R. Experimental and theoretical investigation of heat and mass transfer processes during wood pyrolysis. *Combust. Flame* **2010**, *157*, 481–494. [CrossRef]
2. Haseli, Y.; van Oijen, J.A.; de Goey, L.P.H. Numerical study of the conversion time of single pyrolyzing biomass particles at high heating conditions. *Chem. Eng. J.* **2011**, *169*, 299–312. [CrossRef]
3. Haseli, Y.; van Oijen, J.A.; de Goey, L.P.H. Modeling biomass particle pyrolysis with temperature dependent heat of reactions. *J. Anal. Appl. Pyrol.* **2011**, *90*, 140–154. [CrossRef]
4. Wan, K.; Zhihu, K.; Wang, Z.; He, Y.; Xia, J.; Zhou, Z.; Zhou, J.; Cen, K. Experimental and modeling study of pyrolysis of coal, biomass and blended coal–biomass particles. *Fuel* **2015**, *139*, 356–364. [CrossRef]
5. Atreya, A.; Olszewski, P.; Chen, Y.; Baum, H.R. The effect of size, shape and pyrolysis conditions on the thermal decomposition of wood particles and firebrand. *Int. J. Heat Mass.* **2017**, *107*, 319–328. [CrossRef]

6. Gómez, M.A.; Porteiro, J.; Chapela, S.; Míguez, J.L. An Eulerian model for the simulation of the thermal conversion of a single large biomass particle. *Fuel* **2018**, *22*, 671–681. [CrossRef]
7. Pecha, M.B.; Ramirez, E.; Wiggins, G.M.; Carpenter, D.; Kappes, B.; Daw, S.; Ciesielski, P.N. Integrated particle- and reactor-scale simulation of pine pyrolysis in a fluidized bed. *Energy Fuels* **2018**, *32*, 10683–10694. [CrossRef]
8. Fatehi, H.; Weng, W.; Costa, M.; Li, Z.; Rabaçal Maldén, M.; Bai, X.S. Numerical simulation of ignition mode and ignition delay time of pulverized biomass particles. *Combust. Flame* **2019**, *206*, 400–410. [CrossRef]
9. Fatehi, H.; Weng, W.; Li, Z.; Bai, X.S.; Aldén, M. Recent development in numerical simulations and experimental studies of biomass thermochemical conversion. *Energy Fuels* **2021**, *35*, 6940–6963. [CrossRef]
10. Lu, L.; Gao, X.; Shahnam, M.; Rogers, W.A. Bridging particle and reactor scales in the simulation of biomass fast pyrolysis by coupling particle resolved simulation and coarse grained CFD-DEM. *Chem. Eng. Sci.* **2020**, *216*, 115471. [CrossRef]
11. Lu, L.; Gao, X.; Shahnam, M.; Rogers, W.A. Simulations of biomass pyrolysis using glued-sphere CFD-DEM with 3-D intra-particle models. *Chem. Eng. J.* **2021**, *419*, 129564. [CrossRef]
12. Haseli, Y.; van Oijen, J.A.; de Goey, L.P.H. A detailed one-dimensional model of combustion of a woody biomass particle. *Bioresour. Technol.* **2011**, *102*, 9772–9782. [CrossRef]
13. He, F.; Behrendt, F. A new method for simulating the combustion of a large biomass particle-A combination of a volume reaction model and front reaction approximation. *Combust. Flame* **2011**, *158*, 2500–2511. [CrossRef]
14. Haseli, Y.; van Oijen, J.A.; de Goey, L.P.H. A quasi-steady analysis of oxy-fuel combustion of a wood char particle. *Combust. Sci. Technol.* **2013**, *185*, 533–547. [CrossRef]
15. Torero, J.L.; Gerhard, J.I.; Martins, M.F.; Zanoni, M.A.B.; Rashwan, T.L.; Brown, J.K. Processes defining smouldering combustion: Integrated review and synthesis. *Prog. Energy Combust. Sci.* **2020**, *81*, 100869. [CrossRef]
16. Zhao, P.; García, A.; Burton, T. Initiation and propagation of curved reaction front in solids: Insights into solid combustion and battery thermal runaway. *Combust. Flame* **2022**, *238*, 111951. [CrossRef]
17. Galgano, A.; Di Blasi, C. Modeling wood degradation by the unreacted-core-shrinking approximation. *Ind. Eng. Chem. Res.* **2003**, *42*, 2101–2111. [CrossRef]
18. Wichman, I.S.; Atreya, A. A simplified model for the pyrolysis of charring materials. *Combust. Flame* **1987**, *68*, 231–247. [CrossRef]
19. Chen, Y.; Delichatios, M.A.; Motevalli, V. Material pyrolysis properties, Part I: An integral model for one-dimensional transient pyrolysis of charring and non-charring materials. *Combust. Sci. Technol.* **1993**, *88*, 309–328. [CrossRef]
20. Moghtaderi, B.; Novozhilov, V.; Fletcher, D.; Kent, J.H. An integral model for the transient pyrolysis of solid materials. *Fire Mater.* **1997**, *21*, 7–16. [CrossRef]
21. Spearpoint, M.J.; Quintiere, J.G. Predicting the burning of wood using an integral model. *Combust. Flame* **2000**, *123*, 308–324. [CrossRef]
22. Haseli, Y.; van Oijen, J.A.; de Goey, L.P.H. A simplified pyrolysis model of a biomass particle based on infinitesimally thin reaction front approximation. *Energy Fuels* **2012**, *26*, 3230–3243. [CrossRef]
23. Haseli, Y.; van Oijen, J.A.; de Goey, L.P.H. Reduced model for combustion of a small biomass particle at high operating temperatures. *Bioresour. Technol.* **2013**, *131*, 397–404. [CrossRef] [PubMed]
24. Galgano, A.; Di Blasi, C. Infinite versus finite rate kinetics in simplified models of wood pyrolysis. *Combust. Sci. Technol.* **2005**, *177*, 279–303. [CrossRef]
25. Park, W.C.; Atreya, A.; Baum, H.R. Determination of pyrolysis temperature for charring materials. *Proc. Combust. Inst.* **2009**, *32*, 2471–2479. [CrossRef]
26. Moghtaderi, B.; Novozhilov, V.; Fletcher, D.; Kent, J.H. A new correlation for bench-scale piloted ignition data of wood. *Fire Saf. J.* **1997**, *29*, 41–59. [CrossRef]
27. Spearpoint, M.J.; Quintiere, J.G. Predicting the piloted ignition of wood in the cone calorimeter using an integral model-effect of species, grain orientation and heat flux. *Fire Saf. J.* **2001**, *36*, 391–415. [CrossRef]
28. Yang LChen XZhou, X.; Fan, W. The pyrolysis and ignition of charring materials under an external heat flux. *Combust. Flame* **2003**, *133*, 407–413. [CrossRef]
29. Babrauskas, V. Ignition of wood: A review of the state of the art. In Proceedings of the Interflam 2001, Edinburgh, UK, 17–19 September 2001; Interscience Communications Ltd.: London, UK, 2001; pp. 71–88.
30. Bartlett, A.I.; Hadden, R.M.; Bisby, L.A. A review of factors affecting the burning behaviour of wood for application to tall timber construction. *Fire Technol.* **2019**, *55*, 1–49. [CrossRef]
31. Kashiwagi, T. Experimental observation of radiative ignition mechanisms. *Combust. Flame* **1979**, *34*, 231–244. [CrossRef]
32. Kashiwagi, T. Radiative ignition mechanism of solid fuels. *Fire Saf. J.* **1981**, *3*, 185–200. [CrossRef]
33. Kashiwagi, T. Effects of sample orientation on radiative ignition. *Combust. Flame* **1982**, *44*, 223–245. [CrossRef]
34. Hernández, N.; Fuentes, A.; Reszka, P.; Fernández-Pello, A.C. Piloted ignition delay times on optically thin PMMA cylinders. *Proc. Combust. Inst.* **2019**, *37*, 3993–4000. [CrossRef]
35. Parot, R.; Rivera, J.I.; Reszka, P.; Torero, J.L.; Fuent, A. A simplified analytical model for radiation dominated ignition of solid fuels exposed to multiple non-steady heat fluxes. *Combust. Flame* **2022**, *237*, 111866. [CrossRef]
36. Rhodes, B.T.; Quintiere, J.G. Burning rate and flame heat flux for PMMA in a cone calorimeter. *Fire Saf. J.* **1996**, *26*, 221–240. [CrossRef]
37. Boonmee, N.; Quintiere, J.G. Glowing and flaming autoignition of wood. *Proc. Combust. Inst.* **2002**, *29*, 289–296. [CrossRef]

38. Mikkola, E.; Wichman, I.S. On the thermal ignition of combustible materials. *Fire Mater.* **1989**, *14*, 87–96. [CrossRef]
39. Biot, M.A. New methods in heat flow analysis with application to flight structures. *J. Aeronaut. Sci.* **1957**, *24*, 857–873. [CrossRef]
40. Haseli, Y.; Naterer, G.F. Transient heat conduction in a planar slab with convection and radiation effects. *J. Heat Transf.* **2022**, *144*, 121401. [CrossRef]
41. Lu, H.; Ip, E.; Scott, J.; Foster, P.; Vickers, M.; Baxter, L.L. Effects of particle shape and size on devolatilization of biomass particle. *Fuel* **2010**, *89*, 1156–1168. [CrossRef]
42. Milosavljevic, I.; Oja, V.; Suuberg, E.M. Thermal effects in cellulose pyrolysis: Relationship to char formation processes. *Ind. Eng. Chem. Res.* **1996**, *35*, 653–662. [CrossRef]
43. Haseli, Y.; van Oijen, J.A.; de Goey, L.P.H. Predicting the pyrolysis of single biomass particles based on a time and space integral method. *J. Anal. Appl. Pyrol.* **2012**, *96*, 126–138. [CrossRef]
44. Shafizadeh, F.; Chin, P.P.S. Thermal deterioration of wood. In *Wood Technology: Chemical Aspects*; ACS Symposium Series; Goldstein, I.S., Ed.; American Chemical Society: Washington, DC, USA, 1977; pp. 57–81.
45. Peters, B.; Bruch, C. Drying and pyrolysis of wood particles: Experiments and simulation. *J. Anal. Appl. Pyrol.* **2003**, *70*, 233–250. [CrossRef]
46. Dakka, S.M.; Jackson, G.S.; Torero, J.L. Mechanisms controlling the degradation of poly(methyl methacrylate) prior to piloted ignition. *Proc. Combust. Inst.* **2002**, *29*, 281–287. [CrossRef]
47. Vermesi, I.; Di Domizio, M.J.; Richter, F.; Weckman, E.J.; Rein, G. Pyrolysis and spontaneous ignition of wood under transient irradiation: Experiments and a-priori predictions. *Fire Saf. J.* **2017**, *91*, 218–225. [CrossRef]
48. Boonmee, N.; Quintiere, J.G. Glowing ignition of wood: The onset of surface combustion. *Proc. Combust. Inst.* **2005**, *30*, 2303–2310. [CrossRef]
49. Boonmee, N. Theoretical and Experimental Study of Autoignition of Wood. Ph.D. Thesis, University of Maryland, College Park, MD, USA, 2004.
50. McAllister, S.; Finney, M. Autoignition of wood under combined convective and radiative heating. *Proc. Combust. Inst.* **2017**, *36*, 3073–3080. [CrossRef]
51. Quintiere, J.G. Approximate solutions for the ignition of a solid as a function of the Biot number. *Fire Mater.* **2019**, *43*, 57–63. [CrossRef]